

# Alleviating Voltage Hysteresis by Interconnecting Truncated Octahedral $\text{LiNi}_{0.5}\text{Mn}_{1.5}\text{O}_4$ Cathode Particles Using Exfoliated Graphene

Putri Nadia Suryadi,<sup>[a]</sup> Jotti Karunawan,<sup>[b]</sup> Oktaviardi Bityasmawan Abdillah,<sup>[a, c]</sup> Octia Floweri,<sup>[c, d]</sup> Sigit Puji Santosa,<sup>[e]</sup> Arie Wibowo,<sup>[b, f]</sup> and Ferry Iskandar<sup>\*[a, b, c, e]</sup>

High-voltage spinel  $\text{LiNi}_{0.5}\text{Mn}_{1.5}\text{O}_4$  (LNMO) has been highlighted as one of the most promising cathode materials for next-generation Li-ion batteries. However, its performance is known to have shortcomings, i.e., voltage hysteresis induced by the increasing impedance of LNMO during electrochemical cycling at high voltage operation. This paper demonstrates an innovative design of LNMO cathode materials to alleviate voltage hysteresis by combining unique characteristics of truncated octahedral LNMO with 2D exfoliated graphene (EG). The exposed (100) plane of truncated LNMO particles is known to have superior  $\text{Li}^+$  ion conduction. Meanwhile, the (111) plane is known to have excellent resistance to metal dissolution.

Moreover, it was revealed that the presence of the EG framework as an interconnection aide could significantly improve the charge transfer process, helping to alleviate the voltage polarization. The sample with optimum LNMO-EG composition shows a stable electrochemical performance with a capacity retention of 86.56% after 300 cycles of charge-discharge measurement at 1 C while exhibiting almost 3 times lower voltage hysteresis (0.233 mV/cycle) compared to the pristine LNMO (0.678 mV/cycle). This result demonstrates that combining the uniqueness of truncated LNMO and 2D EG can be a promising strategy to improve the electrochemical performance of LNMO cathode materials for next-generation batteries.

## Introduction

Li-ion batteries (LiB) have been successfully commercialized and widely utilized as energy storage devices, especially for portable electronics. For the last couple of years, they have also been playing a key role as an indispensable component in electric vehicles (EVs) and hybrid EVs (HEVs).<sup>[1]</sup> Among battery components, cathode materials highly contribute to the energy power density of the battery. Several types of cathode material have been developed for LiB application, including layered (e.g.,  $\text{LiCoO}_2$  (LCO) and Ni-based layered cathode), spinel (e.g.,

$\text{LiMn}_2\text{O}_4$  (LMO) and  $\text{LiNi}_{0.5}\text{Mn}_{1.5}\text{O}_4$  (LNMO)), olivine (e.g.,  $\text{LiFePO}_4$  (LFP)), and tavorite (e.g.,  $\text{LiVPO}_4\text{F}$  (LVPF)).<sup>[2]</sup> Among them, spinel LNMO has been considered attractive due to its high operating voltage (around 4.7 V vs.  $\text{Li}/\text{Li}^+$ ), high energy density ( $\sim 650 \text{ Wh kg}^{-1}$ ), and three-dimensional  $\text{Li}^+$  ion migration channel.<sup>[3]</sup> Moreover, the absence of the Co element in the LNMO also gives benefits in terms of lower cost production and lower toxicity.<sup>[4]</sup>

There are two types of LNMO crystal structures, i.e., ordered  $\text{P}4_3\text{3}2$  structure and disordered  $\text{Fd}\bar{3}\text{m}$  which are determined by heat treatment temperature during synthesis.<sup>[5]</sup> The disordered LNMO with a face-centered cubic  $\text{Fd}\bar{3}\text{m}$  structure demonstrates more desirable electrochemical behavior than the ordered one, thanks to the  $\text{Mn}^{3+}$  ions present in the disordered structure, which promotes electronic conductivity and improves  $\text{Li}^+$  ion diffusivity.<sup>[6]</sup> On the other hand, the presence of  $\text{Mn}^{3+}$  ions tends to induce Jahn-Teller distortion and disproportionation reaction ( $2\text{Mn}^{3+} \rightarrow \text{Mn}^{2+} + \text{Mn}^{4+}$ ), leading to Mn dissolution and structural collapse of the cathode materials.<sup>[7]</sup> The dissolved Mn ions will also react with the electrolyte and induce the formation of undesired products in the form of cathode-electrolyte interphase (CEI). This phenomenon will be aggravated by the decomposition of  $\text{LiPF}_6$  electrolytes upon operation at high voltage, resulting in a significant increase in impedance.<sup>[8]</sup> The increase in impedance induces cell polarization within the electrode, which later results in a large voltage hysteresis upon charging/discharging.<sup>[9]</sup> Voltage hysteresis is known as one of the substantial problems in batteries that must be controlled as it leads to a decrease in battery energy density.

[a] P. Nadia Suryadi, Dr. O. Bityasmawan Abdillah, Prof. F. Iskandar  
Department of Physics, Faculty of Mathematics and Natural Sciences, Institut Teknologi Bandung, Jl. Ganesha 10, Bandung 40132, Indonesia  
E-mail: ferry@itb.ac.id

[b] Dr. J. Karunawan, Dr. A. Wibowo, Prof. F. Iskandar  
Research Center for Nanoscience and Nanotechnology (RCNN), Institut Teknologi Bandung, Jl. Ganesha 10, Bandung 40132, Indonesia

[c] Dr. O. Bityasmawan Abdillah, Dr. O. Floweri, Prof. F. Iskandar  
Collaboration Research Center for Advanced Energy Materials, National Research and Innovation Agency – Institut Teknologi Bandung, Jl. Ganesha 10, Bandung 40132, Indonesia

[d] Dr. O. Floweri  
Research Center for Nanotechnology Systems, National Research and Innovation Agency (BRIN), South Tangerang 15314, Banten, Indonesia

[e] Dr. S. Puji Santosa, Prof. F. Iskandar  
National Center for Sustainable Transportation Technology (NCSTT), Institut Teknologi Bandung, Jl. Ganesha 10, Bandung 40132, Indonesia

[f] Dr. A. Wibowo  
Material Science and Engineering Research Group, Faculty of Mechanical and Aerospace Engineering, Jl. Ganesha 10, Bandung 40132, Indonesia

Supporting information for this article is available on the WWW under <https://doi.org/10.1002/batt.202400515>

Some studies reported that LNMO with a truncated octahedral shape demonstrates excellent electrochemical properties, including high ionic conductivity and excellent cycling stability, thanks to its unique morphology.<sup>[10]</sup> The truncated LNMO comes with an octahedral shape with two exposed planes, i.e., (100) and (111) planes. The (100) plane has a dense Li atom arrangement that supports  $\text{Li}^+$  ion transport kinetics, whereas the (111) plane demonstrates a dense atomic arrangement that inhibits Mn dissolution and relieves side reactions at the electrode/electrolyte interface.<sup>[10a,11]</sup> These excellent features make truncated LNMO potential to manifest excellent and stable electrochemical performance. Many researchers also proposed surface modification as a potential way to alleviate the problem of voltage hysteresis in LNMO.<sup>[12]</sup> Several works about LNMO surface modification have been reported, including applying thin layers of metal oxide, polymer, and carbon-based materials as surface modifiers. Conductive carbon-based materials such as carbon nanotubes, carbon black, graphite, and graphene are considered prospective owing to their excellent electronic conductivity, electrochemical inactivity, and abundance in nature.<sup>[13]</sup>

In recent years, it has been reported that graphene-based materials enhance the electrochemical performance of LNMO cathode material thanks to their excellent electronic conductivity, large specific surface area, and their role in limiting direct contact between the LNMO cathode particle and electrolyte species (HF).<sup>[14]</sup> Various graphene-based materials, such as graphene,<sup>[15]</sup> graphene oxide (GO),<sup>[16]</sup> GO aided by chitosan,<sup>[17]</sup> and reduced graphene oxide (rGO),<sup>[18]</sup> have been adopted to modify LNMO and proven to improve its properties. On the other hand, electrochemically exfoliated graphene (EG), which possesses a high electronic conductivity thanks to fewer defects and more aromatic domain in its structure,<sup>[19]</sup> also have the potential to be applied as a surface modifier. Moreover, their small size is beneficial, providing a short pathway for  $\text{Li}^+$  ion,

which ensures the fast ionic transfer between one cathode particle and the other.<sup>[19b]</sup> Thus, EG can potentially be utilized as a coating material for LNMO particles.

In this work, we have examined the use of electrochemically exfoliated graphene (EG) as a surface modifier and interconnection aide for truncated LNMO cathode particles without the addition of any surfactant to promote eco-friendly routes. Adding EG to truncated LNMO synergistically is expected to improve the interparticle connection, thus minimizing the polarization issue. Benefited from interesting features of truncated octahedral LNMO and two-dimensional EG, the sample with optimum LNMO-EG composition could maintain a capacity of 86.56% after 300 cycles at 1 C while exhibiting a lower voltage hysteresis of 0.233 mV/cycle compared to the pristine LNMO of 0.678 mV/cycle. This study not only elucidates the potential mechanism by which EG boosts the electrochemical performance of LNMO but also gives us insight into the eco-friendly and economical routes to prepare the LNMO-EG.

## Results and Discussion

### Structural and Morphology Characterizations

The XRD characterization results of the pristine and EG-modified LNMO samples are exhibited in Figure 1a. Compared to the literature, the XRD patterns of all samples belong to  $\text{Fd}\bar{3}\text{m}$  space group and are well-matched with the standard PDF#80-2162. However, XRD patterns of all samples exhibit a weak peak at  $2\theta = 15.8^\circ$ , which could be attributed to the impurity phase of  $\text{Na}_{0.7}\text{MnO}_{2.05}$  (PDF#27-0751) caused by hydrated Mn–Na oxides ( $\text{Na}_{0.55}\text{Mn}_2\text{O}_4 \cdot 1.5\text{H}_2\text{O}$ ) turning into a layered  $\text{Na}_{0.7}\text{MnO}_{2.05}$  structure after heat treatment.<sup>[20]</sup> The other impurity phase is also detected at  $2\theta = 37.4^\circ$  and  $43.7^\circ$ , which indicates the

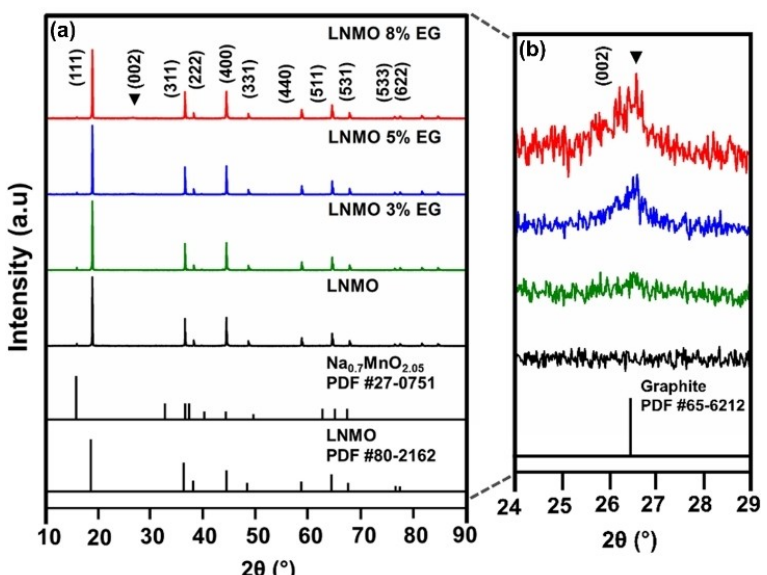


Figure 1. (a) XRD patterns (b) magnified view of (002) diffraction peaks of LNMO and LNMO EG-modified cathode.

existence of the cation-rich rock-salt phase  $\text{Li}_x\text{Ni}_{1-x}\text{O}$ .<sup>[21]</sup> A fine diffraction peak at  $26.5^\circ$  can also be observed from the enlarged XRD pattern (Figure 1b) of EG-modified LNMO samples pattern at  $24^\circ$ – $29^\circ$ , ascribing the existence of graphene-based materials.<sup>[22]</sup>

The effect of EG addition on the structure of LNMO particles was analyzed by Raman spectroscopy (Figure S2). There are two main peaks that can be seen in the Raman spectra

of all samples i.e.,  $\sim 497 \text{ cm}^{-1}$  and  $\sim 636 \text{ cm}^{-1}$ . These peaks are attributed to the stretching vibration modes of Ni–O bonds and symmetric stretching vibration of Mn–O bonds in the  $\text{MnO}_6$  octahedral group, respectively.<sup>[14]</sup> Meanwhile, the presence of peaks with a clear split around  $600 \text{ cm}^{-1}$  indicates that all LNMO samples belong to the disordered space group ( $\text{Fd}\bar{3}\text{m}$ ). These results indicate the EG treatment does not change the

space group of LNMO cathode materials. Then, the modified samples also show the presence of D, G, and 2D peaks, representing the characteristics of exfoliated graphene materials (Figure S2b). The disorder or the defect-induced  $\text{sp}^3$ -bonded carbon is represented by the D peak at  $\sim 1350 \text{ cm}^{-1}$ . Meanwhile, the in-plane vibrational mode of  $\text{sp}^2$  hybridized carbon atoms in the graphene sheet is found at the G peak located at  $\sim 1580 \text{ cm}^{-1}$  and the 2D peak located at  $\sim 2700 \text{ cm}^{-1}$ <sup>[23]</sup> and the formation of few-layer graphene,<sup>[24]</sup> respectively.

Figure 2a–d shows the morphology of the pristine, 3, 5, and 8 wt.% EG-wrapped LNMO samples observed by SEM, respectively. All samples exhibit LNMO particles with a truncated octahedral morphology, exposing (111) and (100) surface planes.<sup>[10a]</sup> Figure 2a depicts the micrometer-sized pristine LNMO particles with a clear and smooth surface. Meanwhile, (Figure 2b–d) shows the modified LNMO samples in which EG looks homogeneously enwrapped LNMO particles and forms a 3D interconnected network. The conductive EG will accelerate the electron movement on the surface of LNMO particles, thus improving the electronic conductivity of the cathode. However, the increase of EG content leads to the thickening of the EG layer on the LNMO surface, which may affect the tortuosity of the  $\text{Li}^+$  diffusion pathway.

### Electrochemical Measurements

Electrochemical measurements of all samples were conducted in a half-cell configuration (vs.  $\text{Li}/\text{Li}^+$ ). Figure 3a shows the result of charge/discharge tests in the voltage range of 3.5–4.8 V at 0.1 C ( $1 \text{ C} = 147 \text{ mA g}^{-1}$ ) at room temperature. All charge-discharge profiles exhibit the presence of three platforms that can be attributed to the disordered structure ( $\text{Fd}\bar{3}\text{m}$ ) of LNMO.

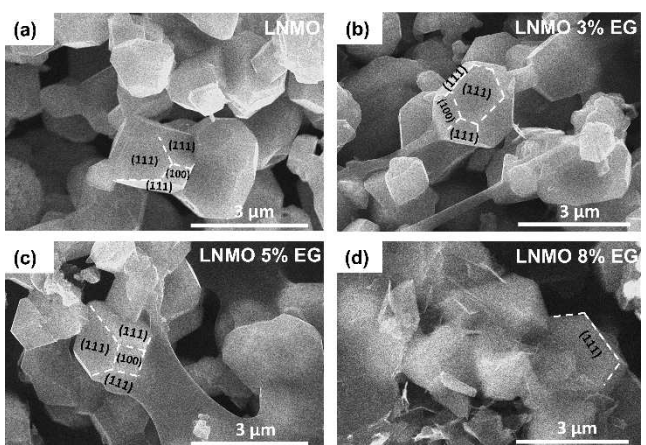


Figure 2. SEM images of the (a) pristine, (b) 3 wt.%, (c) 5 wt.%, and (d) 8 wt.% EG-modified LNMO.

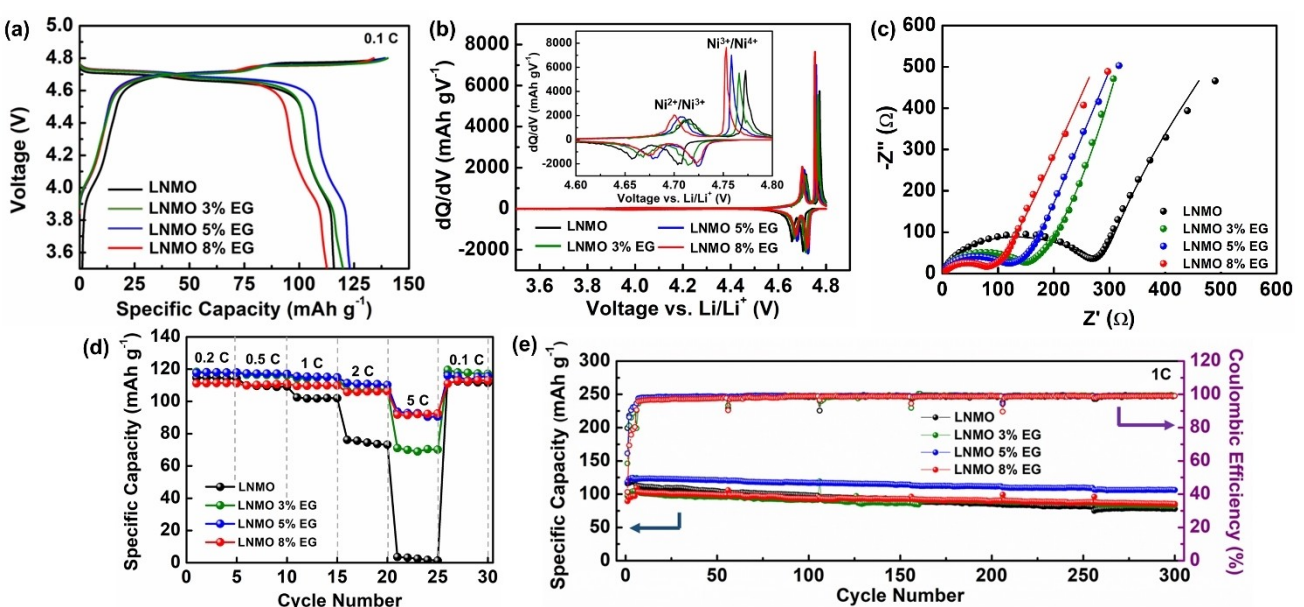


Figure 3. (a) Initial charge-discharge measured at 0.1 C (3.5–4.8 V), (b) dQ/dV profiles with an inset of magnified view of  $\text{Ni}^{2+}/\text{Ni}^{3+}/\text{Ni}^{4+}$  redox couples, (c) Nyquist plots obtained from EIS measurement, (d) rate capability measured at different current densities, and (e) cycling stability after 300 cycles measured at 1 C of LNMO and LNMO-EG composites.

The first one is a small platform located at ~4 V, related to the redox couple of  $Mn^{4+}/Mn^{3+}$ .<sup>[25]</sup> Meanwhile, the two other platforms, which correspond to the redox of  $Ni^{4+}/Ni^{3+}$  and  $Ni^{3+}/Ni^{2+}$ , can be seen at ~4.70 and 4.75 V.<sup>[25]</sup>

Overall, the EG-modified samples do not show significant change in terms of charge-discharge profile compared to the pristine one, confirming that the addition of EG does not affect the fundamental properties of LNMO. The specific discharge capacity of LNMO, LNMO 3% EG, LNMO 5% EG, and LNMO 8% EG samples are 115.85, 119.95, 123.06, and 112.66 mAh g<sup>-1</sup>, respectively. The specific discharge capacity increases with EG content up to 5 wt%. Adding EG content higher than 5 wt% decreased specific discharge capacity, probably because the thick layer of EG inhibits the movement of Li<sup>+</sup> ion. A similar trend can also be observed from the initial Coulombic efficiency (ICE) of the samples. The pristine LNMO, LNMO 3%, LNMO 5%, and LNMO 8% EG samples reveal ICE of 83.30, 85.47, 88.63, and 84.10%, respectively. It is obvious that the modified LNMO samples have higher ICE than the pristine samples. The existence of EG might inhibit the irreversible reactions that happen on the surface of the LNMO cathode at the initial charging process, resulting in the formation of a thinner cathode electrolyte interphase (CEI).<sup>[26]</sup> The LNMO 5% EG sample has the highest ICE among the other samples, which highlights the weight percentage of added EG must impact the electrochemical performance. Despite the improved electrochemical performance up to a certain point, increasing the EG content higher than 5 wt% caused the performance to deteriorate, probably due to the thick layer of EG that inhibits Li<sup>+</sup> ion transfer to and from the cathode particles.

To gain a more comprehensive understanding of the effect of EG addition on the electrochemical properties of LNMO cathodes, the differential capacity vs. voltage (dQ/dV) curves were plotted (Figure 3b). The dQ/dV plots are the result of differentiation of the initial charge-discharge profiles shown in Figure 3a. Two large characteristic oxidation and reduction peaks represent the redox couple of  $Ni^{2+}/Ni^{3+}$  and  $Ni^{3+}/Ni^{4+}$ . It is known that voltage differences ( $\Delta V$ ) between two peaks of  $Ni^{2+}/Ni^{3+}$  and  $Ni^{3+}/Ni^{4+}$  redox couples can be used to determine the cation disordering. The  $\Delta V$  above 50 mV can be attributed to Fd3m disordered structure; meanwhile, a  $\Delta V$  below 30 mV can be attributed to the P4<sub>3</sub>2 ordered structure.<sup>[6b,27]</sup> It can be calculated that the voltage differences of LNMO pristine, LNMO 3% EG, LNMO 5% EG, and LNMO 8% EG are 58, 51, 52, and 53 mV, respectively. This result clearly indicates that all samples have Fd3m structure, which is aligned with the XRD characterization result. The presence of disordered LNMO crystal structure is also indicated by a small oxidation peak at 4.05 V and reduction peak at 4.0 V in the dQ/dV plot of all samples, which originates from the  $Mn^{3+}/Mn^{4+}$  redox couple (Figure S3). Overall, the LNMO-modified sample shows significantly smaller polarization compared to LNMO pristine, indicating that adding EG can alleviate voltage polarization by improving conductivity and facilitating Li<sup>+</sup> ion migration.<sup>[28]</sup>

To understand the impactful effect of the exfoliated graphene network on the electrochemical kinetics of LNMO, EIS measurement was carried out. EIS measurement was performed

in a half-cell coin configuration at room temperature on a freshly assembled cell. The corresponding Nyquist plots are shown in Figure 3c. The Nyquist plots of the four battery cells can be fitted with the equivalent circuit diagram shown in the Supplementary Information, Figure S4. There are some parameters can be extracted from the Nyquist plots, i.e., Ohmic resistance ( $R_\Omega$ ), cathode charge transfer resistance ( $R_{ct}$ ), cathode interface double-layer capacitance (CPE), and the Warburg diffusion ( $Z_w$ ). The semicircle at medium to low frequency is attributed to the direct charge transfer resistance at the interface between the electrode and electrolyte interface ( $R_{ct}$ ).<sup>[29]</sup> The Nyquist plot fitting results show that  $R_{ct}$  of pristine LNMO, LNMO 3% EG, LNMO 5% EG, and LNMO 8% EG is 283.7, 164.5, 138.4, and 94.8 Ω, respectively. LNMO cathodes show smaller  $R_{ct}$  with increased EG content, so adding EG significantly reduces the charge transfer resistance.

The rate capability of the pristine LNMO and EG-modified samples measured under different current densities are presented in Figure 3d. There is no significant capacity decay at a low current density test (i.e., 0.2 – 0.5 C) due to the homogeneous truncated octahedral morphology of LNMO. However, a significant capacity deterioration could be observed at a high current density test (1 – 5 C), especially for the pristine LNMO, which only delivered a discharge capacity of 2.46 mAh g<sup>-1</sup> at 5 C. On the other hand, LNMO 5% EG still delivered 92.05 mAh g<sup>-1</sup> at 5 C. The EG-modified sample possesses a larger capacity at high current density thanks to improved electronic conductivity in the presence of the EG conductive network formed on the surface of LNMO particles.

Figure 3e shows the cycling performance of the half cells measured at 1 C (1 C = 147 mAh g<sup>-1</sup>) with a potential range of 3.5–4.8 V vs. Li/Li<sup>+</sup>. This characterization was conducted after three initial charging and discharging cycles at 0.1 C at room temperature. The capacity retention of the pristine LNMO, LNMO 3% EG, LNMO 5% EG, and LNMO 8% EG after 300 cycles at 1 C was 69.36%, 83.20%, 86.56%, and 85.36%, respectively. Remarkably, the characterization of cycling stability reveals significant differences in capacity retention among the pristine and EG-modified LNMO samples with Coulombic efficiency of over 98% after 300 cycles. Noteworthily, the LNMO 5% EG sample exhibits the best electrochemical stability among the samples.

The evolution of electrode polarization upon cycling was further analyzed to understand the effect of EG addition in alleviating voltage hysteresis in truncated LNMO. Figure 4a shows the comparison of the average voltage between LNMO pristine and LNMO 5% EG upon 300 cycles of charge-discharge measurement, indicating a more stable charge-discharge voltage of the EG-modified LNMO. This result aligns with the plot of voltage hysteresis evolution, which compares LNMO and LNMO 5% EG samples (Figure 4b). The voltage hysteresis of LNMO 5% EG is 0.233 mV/cycle, or ~2.9 times lower than the pristine one (0.678 mV/cycle). Both samples show a relatively low voltage hysteresis aligned to the beneficial truncated octahedral morphology of LNMO micro-particles with the exposed (100) and (111) surface planes. Both surface planes impede the CEI layer's growth owing to low surface energy.<sup>[10a,30]</sup> Further, it

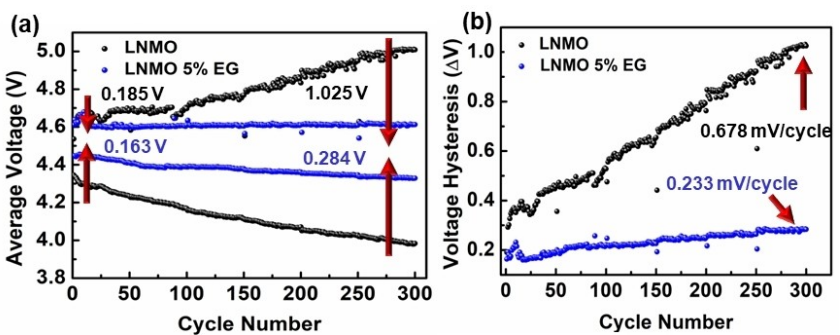


Figure 4. (a) Average voltage of 300 cycle charge-discharge profile, and (b) voltage hysteresis of LNMO and LNMO 5% EG.

should be noted that the additional EG on LNMO not only boosts the electronic conductivity but also plays a role as a cathode protective layer. EG could preserve the surface of LNMO from electrolyte attack at high-voltage operation, which supports the electrochemical performance. This result is validated by the EIS measurement result, which reveals more suppressed CEI formation in the sample LNMO-EG after cycling, as shown in Figure S5. Therefore, the existence of EG on LNMO is beneficial to maintaining the discharge capacity and impeding the CEI growth upon electrochemical cycling.

In addition, to further evaluate the chemical composition on the LNMO cathode surface after cycling, the XPS measurement was conducted. As shown in Figure S6, the decomposition product of organic solvents in electrolytes is revealed from C 1s and O 1s XPS spectra. The deconvolution of C 1s and O 1s spectra of both samples reveals the existence of C–O and C=O peaks, which can be attributed to some electrolyte decomposition products, i.e.,  $\text{Li}_2\text{CO}_3$  and  $\text{RCO}_3\text{Li}$ .<sup>[32]</sup> The presence of EG in the LNMO-EG sample demonstrates prominently lower peak intensities of C 1s and O 1s than that present by pristine LNMO sample, which can be mainly attributed to the smaller amount

of electrolyte decomposition products and generation of thinner CEI layer on LNMO-EG sample. Furthermore, the Li 1s, F 1s, and P 2p XPS spectra were also deconvoluted to analyze the byproduct containing Li salts (Figure 5). The peak intensity comparison of Li 1s and F 1s spectra of both samples reveals the minimal LiF formation on the surface of the LNMO-EG cathode. The larger amount of LiF on the surface of pristine LNMO indicates a massive loss of  $\text{Li}^{+}$  ion at the interface, which leads to capacity degradation and increased charge-transfer resistance.<sup>[33]</sup> In addition, a significant difference can also be observed in the P 2p spectra. The deconvolution of P 2p spectra reveals that LNMO-EG produced only one P-related CEI species, i.e.,  $\text{Li}_x\text{PO}_y\text{F}_z$ , whereas pristine LNMO produced  $\text{Li}_x\text{PF}_y$  and a smaller proportion of  $\text{Li}_x\text{PO}_y\text{F}_z$ . Several studies have reported the advantages of  $\text{Li}_x\text{PO}_y\text{F}_z$ -rich CEI layer on the cathode particle, such as effectively providing protection against the residue of solvent molecules and the highly active cathode surface, improving the conductivity, and enhancing the high voltage resistance of the electrolyte,<sup>[34]</sup> as well as suppressing voltage hysteresis. Therefore, the higher proportion of gener-

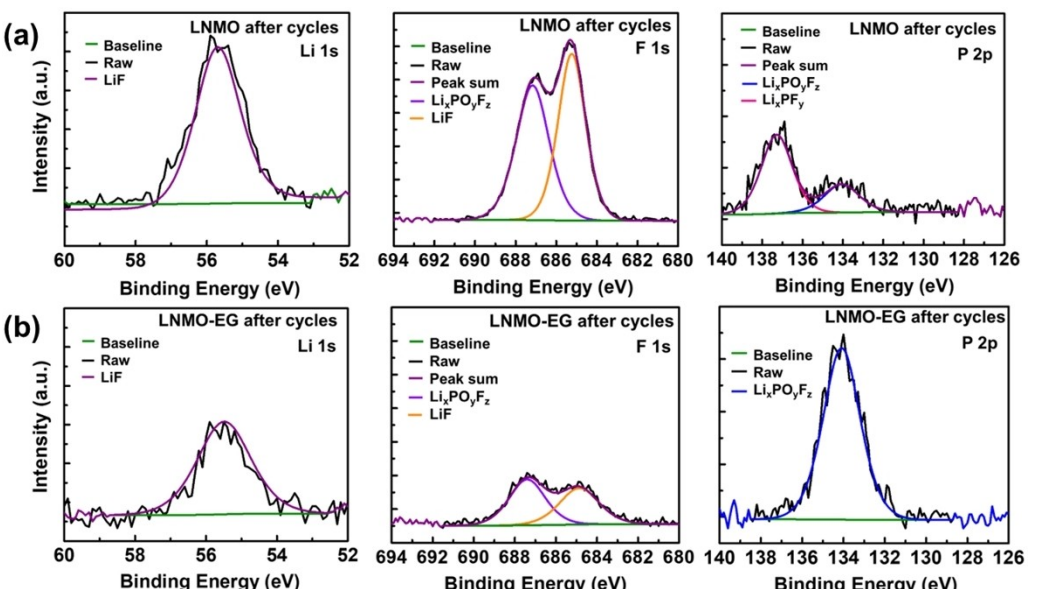


Figure 5. The Li 1s, F 1s, and P 2p XPS spectra profiles of (a) pristine LNMO and (b) LNMO-EG after cycling.

ated  $\text{Li}_x\text{PO}_y\text{F}_z$  in LNMO-EG is favorable and contributes to its superior electrochemical properties.

Galvanostatic intermittent titration technique (GITT) measurement was also employed for deeper electrochemical behavior investigation of the cathode materials. Figure 6a-b shows the GITT plots of pristine LNMO and LNMO 5% EG measured in half-cell configuration. The cells were charged and discharged in steps interfered with by rest periods sufficient for potential equilibration.<sup>[9]</sup> The GITT plot of both samples shows a similar shape and exhibits three plateau regions, revealing the unique voltage profile of LNMO with a disordered structure. However, the GITT curves of the samples show significant differences at the initial charging process. Although both samples demonstrate long voltage relaxation at the early stage of the GITT charging curve, the relaxation during the charging process looks less stable and longer in the pristine sample. This phenomenon is known to be caused by the occurrence of electrolyte oxidation that contributes to the thickening of the CEI layer.<sup>[9,35]</sup> The presence of thicker CEI lengthens the  $\text{Li}^+$  ion diffusion pathway and induces a kinetic barrier to ion movement.<sup>[36]</sup> Consequently, the charge resistance increased along with larger polarization. Inversely, the GITT plot of the LNMO-EG sample represents shorter relaxation during

the charging process, indicating a smaller internal resistance at the initial charging state, which supports the EIS characterization result. The lower internal resistance is caused by EG modification on the surface of LNMO particles that hampers the CEI formation, resulting in a thinner CEI layer. A thin CEI layer will reduce the polarization and increase the  $\text{Li}^+$  ion transfer between the electrode/electrolyte during charging process.

In addition, the electrochemical polarization can be identified by examining a specific point on the charging plateau, as shown in Figure 6c,d. The reduced polarization is further confirmed by a lower iR drop of LNMO 5% EG than the pristine sample, owing to the ability of EG to effectively suppress the side reaction during the electrochemical reaction. Furthermore, lithium-ion diffusion coefficients of LNMO and LNMO 5% EG calculated during the charging and discharging process are depicted in Figure S7. During the charging process, the  $\text{Li}^+$  ion diffusion coefficient values of the LNMO 5% EG sample are larger than the pristine sample, denoting the improved rate capability of the modified sample. This excellent feature can be related to the dual role of exfoliated graphene, i.e., as a conductive agent and protective layer of the LNMO particles.

From the above analysis, the improvement of the electrochemical performance of LNMO particle by adding EG as a surface modifier is comparable to some prior works (Table 1),

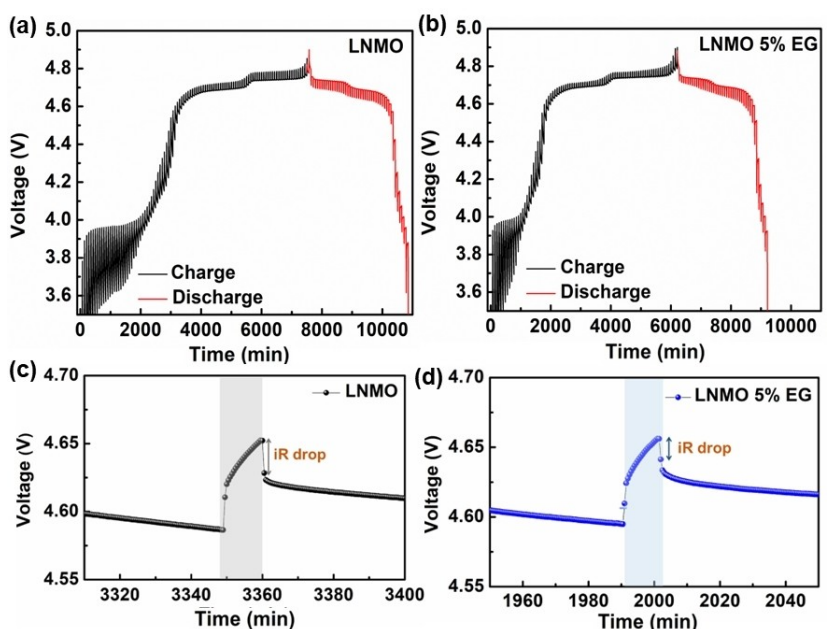


Figure 6. The entire GITT charge-discharge plots of (a) LNMO and (b) LNMO 5% EG, and a single step GITT charging of (c) LNMO and (d) LNMO 5% EG.

**Table 1.** Voltage hysteresis comparison of LNMO modified using EG and other surface modifiers.

Surface modification materials	Electrolyte	Cycling condition in half cell	Voltage hysteresis (mV/cycle)		Ref.
			Bare	Modified	
2D WSe <sub>2</sub>	1 M LiPF <sub>6</sub> in EC/EMC (3:7)	0.5 C/1 C for 400 cycles	~0.70	~0.14	[12a]
Zeolites	1 M LiPF <sub>6</sub> in EC/EMC (3:7)	0.5 C/1 C for 400 cycles	~0.70	~0.39	[12b]
Trimesic acid (TMA)	1 M LiPF <sub>6</sub> in EC/EMC (3:7)	0.5 C/1 C for 400 cycles	~0.70	~0.20	[31]
Exfoliated-Graphene	1 M LiPF <sub>6</sub> in EC/DEC/DMC (1:1:1)	1 C/1 C for 300 cycles	~0.68	~0.23	This work

which can be attributed to the constructive collaboration of truncated LNMO and conductive network of EG. Figure 7 illustrates the possible mechanism of how the interconnection of EG and truncated LNMO could collectively improve the rate and cycling performance of LNMO. The exposed (100) and (111) planes of the truncated LNMO have a significant role in this case. The (100) plane contributes to improving  $\text{Li}^+$  ion transport kinetic due to the densely packed Li atoms on this plane.<sup>[10b]</sup> Whereas the (111) plane possesses high oxygen atom density, preventing Mn dissolution on this surface.<sup>[11]</sup> Besides, both (100) and (111) planes have low surface energy, which suppresses parasitic reactions and the growth of the CEI layer.<sup>[30]</sup> In addition, the presence of EG layers on the surface of truncated octahedral LNMO particles builds an interconnected conductive network, which could boost the electronic transport among the cathode particles and cathode particles to the current collector. Moreover, the EG layers also support extra protection to the surface of LNMO particles by preventing electrolyte attack during high voltage operation.

Furthermore, the improvement of rate capability and cycling performance of LNMO-EG in high current density is supported by some reasons: (i) Good ionic conductivity at (100) surface plane of truncated LNMO, (ii) The contribution of (111) plane of truncated LNMO and EG layers in maintaining structural stability of spinel structure from Mn dissolution and CEI formation, and (iii) EG role in accelerating electron movement from LNMO particles to current collector by forming conductive interconnection. These reasons could explain the homogeneous reaction that prevents the structural collapse under harsh conditions of the high current operation while maintaining cell voltage after long-term cycling in high voltage operation.

## Conclusions

In summary, truncated octahedral LNMO particles with exfoliated graphene (EG) as a surface modifier have been successfully prepared by mixing LNMO particles with EG via a simple mixing method without any surfactant. The experimental results suggested that the EG builds an interconnected framework among truncated octahedral LNMO particles, which can boost the electrochemical performance of the LNMO cathode. The electrochemical performance of the LNMO cathode (cycle performance and rate capability) is substantially enhanced with an appropriate addition of EG (~5 wt%). Further investigations indicate that integrating EG material can reduce the charge transfer resistance, improving the electronic conductivity of LNMO and reducing polarization during charging-discharging, significantly alleviating the voltage hysteresis. Therefore, the strategy to combine the unique morphology of truncated LNMO with surface modification by adding conductive EG in this work not only can be a reasonable approach to enhance the electrochemical performance of LIB but also can give more in-depth insight into interface decoration in an electrochemical system.

## Experimental Section

### Materials

Bare LNMO was synthesized through a simple coprecipitation method using lithium hydroxide ( $\text{LiOH}$ , 98%, Merck, Germany), manganese sulfate monohydrate ( $\text{MnSO}_4 \cdot \text{H}_2\text{O}$ , 99%, Merck, Germany), nickel sulfate hexahydrate ( $\text{NiSO}_4 \cdot 6\text{H}_2\text{O}$ , 99%, Merck, Germany) as precursors, and sodium bicarbonate ( $\text{NaHCO}_3$ , 99.7%, Merck, Germany) as precipitant. All chemicals in the experiment were pro-analytical grade and used without any additional purification.

### Synthesis of LNMO

Stoichiometric amounts of  $\text{MnSO}_4 \cdot \text{H}_2\text{O}$  and  $\text{NiSO}_4 \cdot 6\text{H}_2\text{O}$  were dissolved in 100 mL of DI water. Then, 1 M sodium bicarbonate solution was rapidly poured into the metal sulfate solution, resulting in a turbid solution. The solution was vigorously stirred for 3 hours at room temperature. The resulting precipitate was then collected and washed several times with DI water and ethanol then dried at 65 °C for 10 h.<sup>[37]</sup> To obtain LNMO samples, the carbonate precursors were ground with lithium hydroxide ( $\text{Li:Mn:Ni} = 1.05:1.5:0.5$  molar ratio) for 30 min. The mixture was calcined at 450 °C for 8 h in air, then further heat treated at 900 °C under an  $\text{O}_2$  atmosphere for 12 h. Thereafter, the sample was cooled to 500 °C with the rate of  $3^\circ\text{C min}^{-1}$  and maintained for 1 h to produce the truncated octahedral LNMO materials.

### Synthesis of LNMO-EG

In this work, to prepare EG-modified LNMO cathode materials, EG was previously prepared by an electrochemical exfoliation method, following the procedure reported in our previous work (see supplementary information).<sup>[19b]</sup> The basic characterization results of EG used in this study are illustrated in the supplementary information (Figure S1). The obtained EG powder was dispersed in

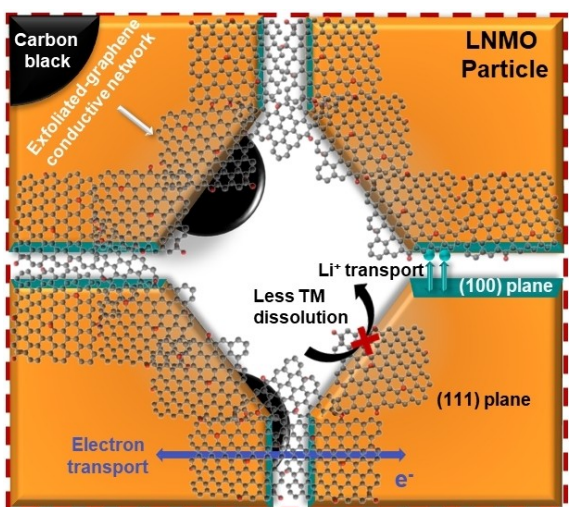


Figure 7. The schematic illustration shows how the EG conductive network may improve the electrochemical properties of truncated octahedral LNMO.

ethanol under an ultrasonic wave for 2 h. Then, the LNMO powder was then appropriately added to the EG solution and stirred at 50°C for 4 h. Finally, the LNMO/EG mixture was collected and vacuum dried at 90°C overnight. The prepared EG-modified LNMO samples which contained 3 wt.%, 5 wt.%, and 8 wt.% of EG were labelled as LNMO 3% EG, LNMO 5% EG, and LNMO 8% EG, respectively.

## Material Characterizations

The crystal structure of all the synthesized samples was examined using X-ray diffraction (XRD, Bruker D8 Advance) with Cu K $\alpha$  radiation of 1.5406 Å within 20 range of 10–90°. Meanwhile, Raman Spectroscopy (Modular Horiba Jobin Yvon type iHR320, Horiba) was utilized to investigate the phase composition, and a scanning electron microscope (SEM, Hitachi SU3500) was utilized to observe the morphology of the samples. The chemical composition at the electrode surface was identified by X-Ray photoelectron spectroscopy (XPS, Thermo Scientific K-Alpha).

## Electrochemical Measurements

The cathode sheets were fabricated by firstly mixing 80 wt.% active material (pristine LNMO, 3, 5, or 10 wt% LNMO@EG), 10 wt.% carbon black, and 10 wt.% poly(vinylidene fluoride) (PVDF, Li-ion battery grade, MTI Corp., USA) binder to form a homogeneous slurry utilizing N-methyl-2-pyrrolidone (NMP, Li-ion battery grade, MTI Corp., USA) as a solvent. Afterward, the slurry was spread on an aluminum foil current collector and vacuum dried at 100°C for 12 h. The dried cathode sheets were then cut into discs of 1.6 cm with mass loading of active material was 2–3 mg cm<sup>-2</sup>. Then, all components were assembled into a CR2032-type coin cell in an Ar-filled glovebox (H<sub>2</sub>O and O<sub>2</sub> concentrations under 0.1 ppm) with Li metal as anode, Celgard 2400 as a separator, and 1 M LiPF<sub>6</sub> (EC:DEC:DMC=1:1:1 v/v) as electrolyte. The electrochemical performances of coin cells were then evaluated from 3.5 to 4.8 V using a battery testing system (Neware BTS4000). Meanwhile, the Galvanostatic Intermittent Titration Technique (GITT) test was performed at a rate of 0.1 C with 10 min of the galvanostatic stage and 1 h of the relaxation stage. The electrochemical impedance spectra (EIS) measurements were carried out using a potentiostat (Parstat 3000, Ametek) over a frequency range of 100 kHz to 0.1 Hz.

## Acknowledgements

This work was fully supported by Riset Unggulan ITB Grant from Institut Teknologi Bandung Fiscal Year 2024 No. 959/IT1.B07.1/TA.00/2024. P.N.S and O.B.A would like to thank the Ministry of Finance, Indonesia, through the Endowment Fund for Education (LPDP) for their doctoral scholarship. We also acknowledge the financial support from Program Talenta Unggul P/PP 2024, managed by The Institute for Science and Technology Development (LPIT), Institut Teknologi Bandung.

## Conflict of Interests

The authors declare no conflict of interest.

## Data Availability Statement

Research data are not shared.

**Keywords:** Electrochemistry · Graphene · Surface modification · Spinel LiNi<sub>0.5</sub>Mn<sub>1.5</sub>O<sub>4</sub> · Voltage hysteresis

- [1] a) A. Manthiram, *Nat. Commun.* **2020**, *11*, 1550; b) J. Karunawan, O. B. Abdillah, O. Floweri, M. P. Aji, S. P. Santosa, A. Sumboja, F. Iskandar, *Batteries* **2023**, *9*, 31.
- [2] P. N. Suryadi, J. Karunawan, O. Floweri, F. Iskandar, *J. Energy Storage* **2023**, *68*, 107634.
- [3] R. Santhanam, B. Rambabu, *J. Power Sources* **2010**, *195*, 5442–5451.
- [4] F. Li, Z. Xu, Q. Sun, D. Hong, C. Y. Xu, Y. Wang, H. T. Fang, *ACS Appl. Mater. Interfaces* **2019**, *11*, 35667–35674.
- [5] a) X. Yu, W. A. Yu, A. Manthiram, *Small Methods* **2021**, *5*, 2001196; b) D. Liu, J. Hamel-Paquet, J. Trottier, F. Baray, V. Gariépy, P. Hovington, A. Guerfi, A. Mauger, C. M. Julien, J. B. Goodenough, K. Zaghib, *J. Power Sources* **2012**, *217*, 400–406; c) M. Hu, X. Pang, Z. Zhou, *J. Power Sources* **2013**, *237*, 229–242; d) J. Song, D. W. Shin, Y. Lu, C. D. Amos, A. Manthiram, J. B. Goodenough, *Chem. Mater.* **2012**, *24*, 3101–3109.
- [6] a) Y. Xue, L.-L. Zheng, J. Wang, J.-G. Zhou, F.-D. Yu, G.-J. Zhou, Z.-B. Wang, *ACS Appl. Energ. Mater.* **2019**, *2*, 2982–2989; b) H. Sun, A. Hu, S. Spence, C. Kuai, D. Hou, L. Mu, J. Liu, L. Li, C. Sun, S. Sainio, D. Nordlund, W. Luo, Y. Huang, F. Lin, *Adv. Funct. Mater.* **2022**, *32*, 2112279.
- [7] T. Liu, A. Dai, J. Lu, Y. Yuan, Y. Xiao, L. Yu, M. Li, J. Gim, L. Ma, J. Liu, C. Zhan, L. Li, J. Zheng, Y. Ren, T. Wu, R. Shahbazian-Yassar, J. Wen, F. Pan, K. Amine, *Nat. Commun.* **2019**, *10*, 4721.
- [8] R. Zhao, L. Li, T. Xu, D. Wang, D. Pan, G. He, H. Zhao, Y. Bai, *ACS Appl. Mater. Interfaces* **2019**, *11*, 16233–16242.
- [9] B. Li, M. T. Sougrati, G. Rousse, A. V. Morozov, R. Dedryvère, A. Iadecola, A. Senyshyn, L. Zhang, A. M. Abakumov, M.-L. Doublet, J.-M. Tarascon, *Nat. Chem.* **2021**, *13*, 1070–1080.
- [10] a) J. Karunawan, P. N. Suryadi, L. Mahfudh, S. P. Santosa, A. Sumboja, F. Iskandar, *Energy Fuels* **2023**, *37*, 754–762; b) B. Chen, L. Ben, Y. Chen, H. Yu, H. Zhang, W. Zhao, X. Huang, *Chem. Mater.* **2018**, *30*, 2174–2182; c) H. Liu, R. Kloepsch, J. Wang, M. Winter, J. Li, *J. Power Sources* **2015**, *300*, 430–437; d) J. Karunawan, L. Mahfudh, S. P. Santosa, F.-M. Wang, A. Sumboja, F. Iskandar, *J. Energy Storage* **2024**, *97*, 112883.
- [11] W. Sun, Y. Li, K. Xie, S. Luo, G. Bai, X. Tan, C. Zheng, *Nano Energy* **2018**, *54*, 175–183.
- [12] a) S. Maiti, R. Konar, H. Sclar, J. Grinblat, M. Talianker, M. Tkachev, X. Wu, A. Kondrakov, G. D. Nessim, D. Aurbach, *ACS Energy Lett.* **2022**, *7*, 1383–1391; b) S. Maiti, H. Sclar, X. Wu, J. Grinblat, M. Talianker, A. Kondrakov, B. Markovsky, D. Aurbach, *Energy Storage Mater.* **2023**, *56*, 25–39.
- [13] a) K.-C. Jiang, X.-L. Wu, Y.-X. Yin, J.-S. Lee, J. Kim, Y.-G. Guo, *ACS Appl. Mater. Interfaces* **2012**, *4*, 4858–4863; b) Z. Yu, L. Jiang, *Solid State Ionics* **2018**, *325*, 12–16; c) T. Hwang, J. K. Lee, J. Mun, W. Choi, *J. Power Sources* **2016**, *322*, 40–48.
- [14] H. Chen, P. He, M. Li, Y. Wen, G. Cao, J. Qiu, H. Ming, P. Zhao, S. Zhang, *ACS Appl. Energ. Mater.* **2021**, *4*, 5963–5972.
- [15] C. Gao, H. Liu, S. Bi, S. Fan, X. Meng, Q. Li, C. Luo, *J. Materiomics* **2020**, *6*, 712–722.
- [16] X. Fang, M. Ge, J. Rong, C. Zhou, *J. Mater. Chem. A* **2013**, *1*, 4083–4088.
- [17] C. Gao, H. Liu, S. Bi, S. Fan, Q. Liu, H. Li, L. Cao, C. Luo, *J. Phys. Chem. C* **2020**, *124*, 18847–18858.
- [18] M. Mo, H. Chen, X. Hong, K. S. Hui, C. Ye, K. Lai, *J. Mater. Sci.* **2017**, *52*, 2858–2867.
- [19] a) J. Cao, P. He, M. A. Mohammed, X. Zhao, R. J. Young, B. Derby, I. A. Kinloch, R. A. W. Dryfe, *J. Am. Chem. Soc.* **2017**, *139*, 17446–17456; b) O. B. Abdillah, O. Floweri, M. A. Irham, A. H. Aimon, T. Ogi, F. Iskandar, *Energy Fuels* **2022**, *36*, 14453–14463.
- [20] J. Mou, H. Wu, Y. Deng, L. Zhou, Q. Zheng, J. Liao, D. Lin, *J. Solid State Electrochem.* **2017**, *21*, 2849–2858.
- [21] a) Y. Qian, Y. Deng, L. Wan, H. Xu, X. Qin, G. Chen, *J. Phys. Chem. C* **2014**, *118*, 15581–15589; b) W. Li, B. Song, A. Manthiram, *Chem. Soc. Rev.* **2017**, *46*, 3006–3059.
- [22] S. J. R. Prabakar, Y.-H. Hwang, B. Lee, K.-S. Sohn, M. Pyo, *J. Electrochem. Soc.* **2013**, *160*, A832.
- [23] a) A. C. Ferrari, D. M. Basko, *Nat. Nanotechnol.* **2013**, *8*, 235–246; b) J.-B. Wu, M.-L. Lin, X. Cong, H.-N. Liu, P.-H. Tan, *Chem. Soc. Rev.* **2018**, *47*, 1822–1873.

- [24] A. C. Ferrari, J. C. Meyer, V. Scardaci, C. Casiraghi, M. Lazzeri, F. Mauri, S. Piscanec, D. Jiang, K. S. Novoselov, S. Roth, A. K. Geim, *Phys. Rev. Lett.* **2006**, *97*, 187401.
- [25] K. Mukai, J. Sugiyama, *J. Electrochem. Soc.* **2010**, *157*, A672.
- [26] J.-H. Shim, Y.-M. Kim, M. Park, J. Kim, S. Lee, *ACS Appl. Mater. Interfaces.* **2017**, *9*, 18720–18729.
- [27] R. Qiao, L. A. Wray, J.-H. Kim, N. P. W. Pieczonka, S. J. Harris, W. Yang, J. *Phys. Chem. C* **2015**, *119*, 27228–27233.
- [28] X. He, G. Han, S. Lou, L. Du, X. Xu, C. Du, X. Cheng, P. Zuo, Y. Ma, H. Huo, G. Yin, *J. Electrochem. Soc.* **2019**, *166*, A1038.
- [29] a) W. Yang, W. Yang, B. Sun, S. Di, K. Yan, G. Wang, G. Shao, *ACS Appl. Mater. Interfaces.* **2018**, *10*, 39695–39704; b) J. Zhang, G. Sun, Y. Han, F. Yu, X. Qin, G. Shao, Z. Wang, *Electrochim. Acta* **2020**, *343*, 136105.
- [30] E. Lee, K. A. Persson, *Nanotechnology* **2014**, *25*, 159501.
- [31] S. Maiti, H. Sclar, J. Grinblat, M. Talianker, Y. Elias, X. Wu, A. Kondrakov, D. Aurbach, *Small Methods* **2022**, *6*, 2200674.
- [32] E. Seok, M. Kim, S. Lee, J. Park, M. Ku, H. Lim, Y. Lee, S. Yu, W. Choi, *Chem. Eng. J.* **2023**, *453*, 139737.
- [33] X. Cai, N. Zhang, J. Wang, X. Zhou, F. Xu, H. Ding, P. Wang, L. Song, J. Huang, X. Fu, X. Cui, C. Yang, S. Li, *Mater. Des.* **2023**, *225*, 111548.
- [34] S. Wu, C. Li, J. Zhang, P. Wang, D. Zhao, Y. Quan, J. Sun, X. Cui, S. Li, *iScience* **2023**, *26*, 107052.
- [35] G. Assat, C. Delacourt, D. A. D. Corte, J.-M. Tarascon, *J. Electrochem. Soc.* **2016**, *163*, A2965.
- [36] Z. A. Qureshi, M. E. S. Ali, R. A. Shakoor, S. AlQaradawi, R. Kahraman, *Ceram. Int.* **2024**, *50*, 17818–17835.
- [37] S. Li, G. Ma, B. Guo, Z. Yang, X. Fan, Z. Chen, W. Zhang, *Ind. Eng. Chem. Res.* **2016**, *55*, 9352–9361.

---

Manuscript received: July 31, 2024  
Revised manuscript received: October 17, 2024  
Accepted manuscript online: October 20, 2024  
Version of record online: November 13, 2024

---